THE ASTROPHYSICAL JOURNAL, 554:368–382, 2001 June 10
© 2001. The American Astronomical Society. All rights reserved. Printed in U.S.A.

FAR-ULTRAVIOLET OBSERVATIONS OF FLARES ON THE dM0e STAR AU MICROSCOPII

RICHARD D. ROBINSON
Computer Sciences Corporation, Civil Group; and Institute for Astrophysics and Computational Science, Catholic University of America; robinson@opal.gsfc.nasa.gov

JEFFREY L. LINSKY
Joint Institute for Laboratory Astrophysics, University of Colorado, Campus Box 440, Boulder, CO 80309-0440; and National Institute of Standards and Technology, A903 Administration Building, Gaithersburg, MD 20899-0001; jlinsky@jila.colorado.edu

BRUCE E. WOODGATE
Laboratory for Atmospheric and Space Physics, University of Colorado, Campus Box 440, Boulder, CO 80309-0440; and NASA Goddard Space Flight Center, Code 681, Goddard Space Flight Center, Greenbelt, MD 20771; woodgate@stars.gsfc.nasa.gov

AND

JOHN G. TIMOTHY
Nightsen, Inc., 30 Fresno Road, Warwick, RI 02886-1407; gethyn@nightsen.com
Received 2000 March 31; accepted 2001 February 1

ABSTRACT

We report on far-ultraviolet (FUV) observations of flares on the dM0e star AU Microscopii obtained on 1998 September 6 with the Space Telescope Imaging Spectrograph onboard the *Hubble Space Telescope*. The data consist of medium-resolution echelle spectra covering the wavelength region from 1170 to 1730 Å with a spectral resolution of $\lambda/\Delta\lambda = 45{,}800$. The observations were obtained using the TIME-TAG observing mode in which the time and position of each detected photon is recorded. This allows a study of variability that is constrained only by counting statistics. During a total on-source time of 10,105 s, we observed numerous microflare bursts as well as four well-defined flare events. These flares lasted between 10 s and 3 minutes and were most easily detected in the FUV continuum and the Si IV and C IV resonance lines. Variations in both the cooler (e.g., Lyα, C II, O I) and hotter (O V, N V, Fe XXI) emission lines were much less pronounced. We examined the physical characteristics of the flare events, including the time history of the wavelength-integrated fluxes in the continuum and the various emission lines. In particular, we searched for, but did not find, evidence for increased emission in the red wing of the Lyα line, which would indicate the presence of moderately energetic proton beams. We integrated the emission over the entire time of major flare activity to investigate the average line and continuum properties of the time-averaged spectrum, including flows and turbulence as a function of temperature. We also considered the shape of the FUV continuum, which may actually be caused by the enhancement of numerous weak emission lines. Unfortunately, none of the events were strong enough to allow a detailed examination of line profiles as a function of time.

Subject headings: stars: activity — stars: flare — stars: late-type — ultraviolet: stars

1. INTRODUCTION

Stellar flares are explosive events that occur near the surface of magnetically active stars. Although progress has been made in the understanding of these events through optical, radio, and X-ray photometry, there is still relatively little known about the physical processes occurring in the bursts, and most of the existing flare models are based on observations of solar events. The relative faintness of the stars at short wavelengths (<4000 Å), where most of the flare effects are seen in dMe stars, and the rapid timescale of the events, where fluxes often vary significantly in seconds, limit our ability to obtain high-quality spectra that adequately sample the flare time history. Such spectra, however, are the key to our understanding of the flare physics.

A particularly significant spectral region is the UV, which contains important resonance lines that sample plasma at temperatures between 10^4 and greater than 2×10^5 K. These emission lines are important probes of the transition region and upper chromosphere, where much of the flare energy is deposited. The UV continuum, which is formed exclusively above the photosphere, also provides important diagnostic information about the temperature minimum through the middle chromosphere. Most of the early UV observations of flares on M dwarfs were obtained with the *IUE* satellite (see, e.g., Byrne 1989). However, the low sensitivity and long readout time of the *IUE* restricted the observations to long exposure times at low spectral resolution, which gave at best the average conditions during the flare.

It was not until the launch of the *Hubble Space Telescope* (*HST*), with its larger collecting area and more sensitive instruments, that high-quality UV observations of flare stars could be obtained. Even so, the high demand for observing time has limited the number of *HST* flare observations to a relative handful. For example, Robinson et al. (1995) and Robinson, Carpenter, & Percival (1999) used the high-speed photometer to study the UV photometric variations of the stars YZ CMi (dM4.5e) and CN Leo (dM8e) in the wavelength range 2000–2800 Å. These observations showed that the UV flares are more impulsive than their optical counterparts, with little or no thermal phase. The larger events were found to be composed of shorter duration bursts, with lifetimes ranging from ~5 to 30 s. There is also evidence for a population of microflares whose numbers are much more numerous than would be predicted from an extrapolation of the frequency-energy relation derived from the larger UV and optical flares. This lends support to the idea that microflares may be a viable means

of heating the stellar corona. Bookbinder, Walter, & Brown (1992) reported observations of a flare on AD Leo (dM4e) taken with the Goddard High Resolution Spectrograph (GHRS) that showed evidence for downflows with velocities up to 1800 km s^{-1}, confirming earlier indications of large velocities seen in the optical (e.g., Houdebine et al. 1993). Later, Woodgate et al. (1992) discovered evidence for proton beams during a flare on AU Mic (dM0.5e) through observations of the Lyα line profile. Follow-up observations on YZ CMi (Robinson et al. 1993) failed to detect evidence for the proton beam but did manage to provide upper limits to the energy carried by such a beam and concluded that it was not the major source of energy transport during the observed flare. Finally, Linsky & Wood (1994) detected a substantial broadening of the Si IV lines as well as significant shifts in the line profile during a flare on AU Mic observed with the GHRS. They proposed that this broadening may be the result of magnetic reconnections within the transition region rather than in the corona, as commonly assumed for the Sun (see, e.g., Antonucci 1989).

In this paper we describe flare observations of AU Mic (Gliese 830) obtained with the Space Telescope Imaging Spectrograph (STIS). These were taken with the echelle grating and are the highest resolution UV spectra ever taken of stellar flares. A particular advantage of the observations is that they were made using the TIME-TAG observing mode, in which the position and time of each detected photon is recorded individually. This allows the observer to reconstruct the time history with any desired temporal resolution. In a companion paper (Pagano et al. 2000, hereafter Paper I) we investigate the quiescent spectrum of AU Mic obtained from this data set by summing 9200 s of observations from which the obvious flare events had been removed. In Paper I we identify 142 emission lines from 28 atomic species formed at temperatures ranging from 10^4 to 10^7 K. One intriguing result of this analysis is a discrepancy between plasma densities derived using the O IV] λ1406/λ1401 line ratio and those deduced by comparing the emission measure loci of these spin-forbidden lines with the emission measure computed using permitted lines. We found that this discrepancy could be resolved if we assume that the emission comes from two distinct types of atmospheric structures, one having relatively low density ($\sim 6 \times 10^{10}$ cm^{-3}) but covering a large surface area and the other having a much larger density ($\sim 5 \times 10^{11}$ cm^{-3}) but occupying a very small area. We suggested that the large, low-density regions corresponded to a stellar plage, while the small, dense regions were microflares. This idea is consistent with the multicomponent nature of the stronger emission lines (e.g., C II, Si IV, and C IV), which have relatively narrow cores and broad, slightly redshifted wings.

In § 2 we describe the observations and data reduction procedures. Section 3 then discusses the dynamics of the flares by examining the time histories of the continuum and emission-line fluxes. In § 3.1 we search the data for all statistically significant flux enhancements and determine the occurrence rate versus energy for these enhancements. In § 3.2 we examine the timing and intensity relationships between the continuum and emission-line fluxes for all of the observed flares, with special emphasis on the smaller, simpler events. This section also searches for bulk flows during the flares by looking for changes in the line profiles of the strongest emission lines. Section 3.3 then presents a search for signatures of proton beams, while § 3.4 investigates the properties of the hot coronal plasma monitored by the Fe XXI line at 1354 Å. In § 4 we combine all of the data taken during times of pronounced flare activity to produce a high-quality spectrum representative of average flare conditions. Using this spectrum, we examine the line profiles for evidence of bulk flows and turbulence (§ 4.1), determine the flare emission measure distribution (§ 4.2), examine the characteristics of the far-ultraviolet (FUV) continuum (§ 4.3), and investigate the density of the flaring plasma (§ 4.4). In § 5 we summarize the observations and compare our results with those found in other flare events.

2. OBSERVATIONS AND DATA REDUCTION

The observations for this study were obtained on 1998 September 6 using the STIS onboard the *HST* (Program 7556). Medium-resolution ($\lambda/\Delta\lambda = 45{,}800$) echelle spectra covering the wavelength region from 1170 to 1730 Å were obtained using the E140M grating, the square 0.″2 aperture, and the FUV MAMA detector. The observations were taken using the TIME-TAG observing mode, in which the time and position of each detected photon are recorded individually. This allows an analysis of the spectral variability that is limited only by the counting statistics of the data. The data were obtained over four consecutive spacecraft orbits (each 96 minutes in duration) and contain 10,105 s of on-source observing time.

We first examined the data by binning the total number of counts received into 5 s duration intervals. The results for each of the orbits are shown in Figure 1. These plots show three obvious flare events during orbit 1 (at 550–680, 750–1050, and 1620–1750 s) and a less pronounced event during orbit 2, at 2370–2540 s. There are also significant short-term variations (more easily seen in individual spectral features; see § 3.1) that are the result of microflare events.

While the nonflaring background during orbit 1 was constant at about 350 counts bin^{-1}, we note that the background shows a monotonic increase with time during subsequent orbits. This was caused by an increase in detector background noise with increasing spacecraft temperature. This background was measured in the inner-order

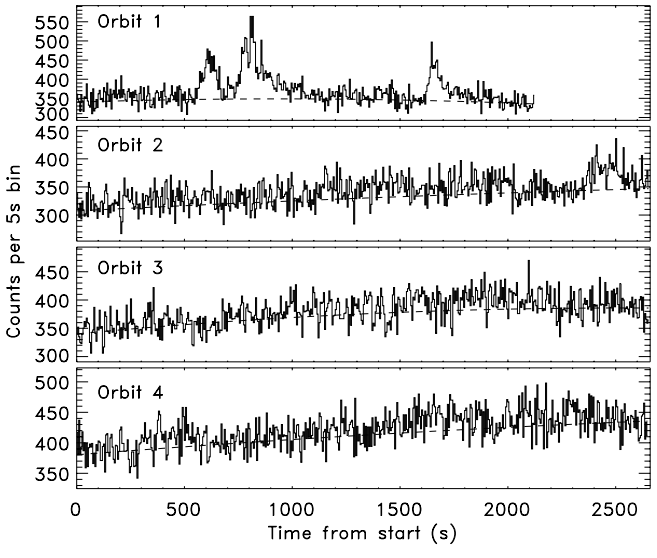


FIG. 1.—Total number of counts detected by the MAMA detector during 5 s intervals as a function of time for each of the four *HST* orbits. Each orbit takes 96 minutes (5760 s) to complete.

portions of the detector and removed during the data analysis.

The entire data set was then integrated over the 9200 s that were not affected by the obvious flares. This yielded a high-quality spectrum that represents the "quiescent" state of the star and has been discussed in Paper I. This data set was also used to establish a mapping between wavelength and position on the echelle image. All data that occurred during the larger flare events were then integrated, producing an average flare spectrum (see § 4). This spectrum showed the total range of wavelengths for each of the emission lines that were affected by the flare. With this information we were able to establish a window on the image that was expected to contain all counts originating from any given emission line.

3. TIME VARIATIONS

To examine the time variations in the line and continuum fluxes, we started by using the TIME-TAG data to generate a sequence of echellogram images, each containing data obtained within a 1 s time interval. The integrated number of counts within 27 separate spectral features was then extracted from each image and stored in a database. In most cases these spectral features represented a single emission line, such as Lyα λ1216, C IV λ1548, or O I λ1306. In several cases the fluxes represent the sum over an entire multiplet (e.g., C III [UV4] near 1176 Å or He II [UV12] near 1640 Å). The intensities in the red and blue wings of Lyα were also extracted for use in a search for proton beams (see § 3.3). The sum total of counts from the spectral features and the expected detector background was subtracted from the total number of counts within the image to give an estimate of the continuum intensity.

A summary of the flux variations for orbit 1, which contains most of the larger flares observed, is presented in Figure 2. To reduce the noise, we have combined the fluxes of lines with similar formation temperatures and binned the time sequence to 10 s intervals. In this plot hot lines include Fe XXI, N V, O V, Si III, Si IV, C III, C IV, and He II, while cool lines are C I, C II, and O I. The figure clearly shows that flux variations are much more pronounced in the continuum and the hot lines than in the cool lines. This result is confirmed by the emission measure analysis presented in § 4.2, which shows that the emission measure in these flares peaks at temperatures near 10^5 K. An examination of the Lyα fluxes shows no significant variations during the flare events. This is probably due to the weak nature of the flares, since pronounced Lyα enhancements have previously been seen in strong flare events observed with the *IUE* (e.g., Linsky et al. 1989; Hawley & Pettersen 1991).

The complex time variations during a flare event are illustrated in Figures 3 and 4, which show the fluxes for emission lines formed at different temperatures during the first two flares of orbit 1. The first event, starting at 560 s into the

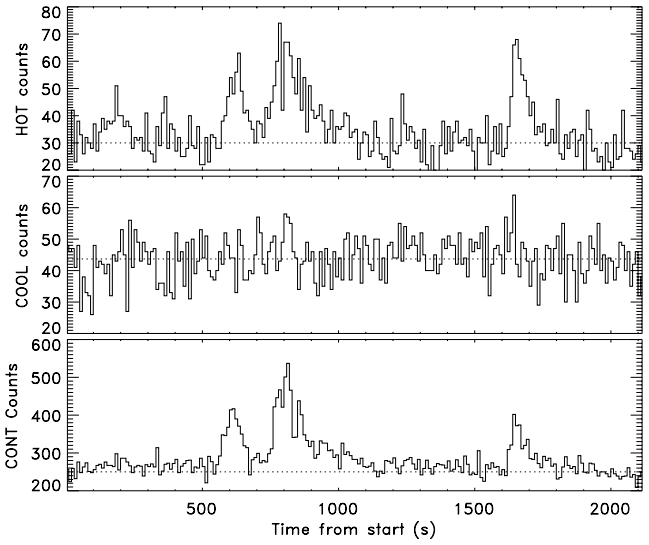


FIG. 2.—Total number of counts detected during 10 s intervals in various emission lines and the continuum during orbit 1. Hot lines included Fe XXI, N V, O V, Si III, Si IV, C III, C IV, and He II. Cool lines included C I, C II, and O I.

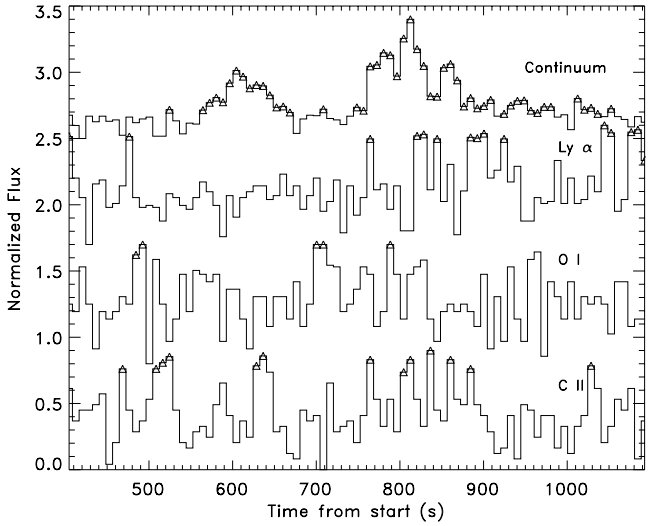


FIG. 3.—Wavelength-integrated fluxes during 10 s sampling intervals for the continuum and the strongest chromospheric emission lines during the first two flare events in orbit 1. The fluxes have been normalized to their average value and displaced vertically for clarity. All samples having a 3 σ deviation from the average are marked with a triangle.

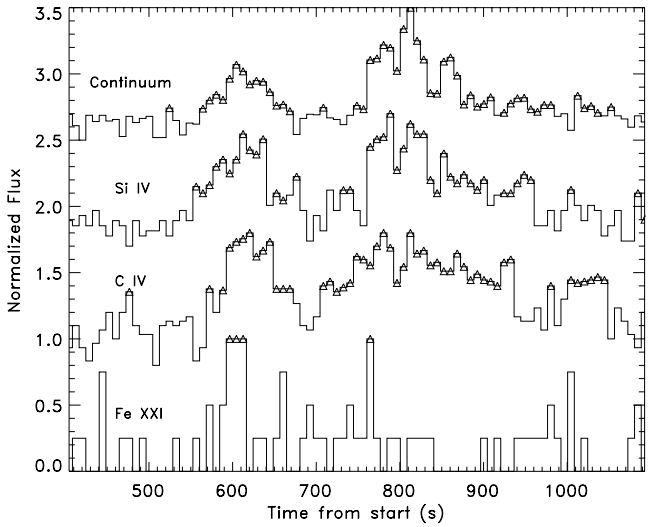


FIG. 4.—Wavelength-integrated fluxes for the continuum, the strongest transition region lines, and the coronal Fe XXI line. The details are identical to those in Fig. 3.

time sequence, showed a gradual increase over about 40 s in both the continuum and Si IV (UV1) lines but a more impulsive increase in the C IV (UV1) lines at 590 s, which was accompanied by an impulsive, short-lived increase in the Fe XXI flux. In the second flare, starting at 700 s, the situation was reversed in that the C IV had a gradual increase covering 70 s, while the continuum and Si IV lines showed a simultaneous impulsive enhancement at 760 s, also in association with an impulsive Fe XXI increase. The C II (UV1) and C III (UV4) lines show relatively small variations during these flares. This is somewhat surprising, since the C III lines are thought to formed at a similar temperature as the Si IV (UV1) lines.

3.1. *Identifying Flare Events*

While the larger flares are very obvious in the time series shown in Figure 1, there are times outside of these events when moderately strong, short-duration bursts are seen. To check the reality of these events, we performed a statistical analysis similar to that used by Robinson et al. (1995, 1999) in searching for microflare events in UV photometric data. We started with the 1 s resolution time sequences for the wavelength-integrated fluxes of the continuum and the strongest emission lines in the spectrum, including Lyα, O I, C II, C IV, Si IV, and He II (see § 3). In all cases the integrated fluxes include all lines within the given multiplet. These time sequences were then binned into intervals ranging from 1 to 15 s, and the number of counts in each bin (C) was compared with an average number C_A derived by fitting a first-order polynomial to the time sequence. If a bin contained counts more than 2 standard deviations above the mean, i.e., $C > C_A + 2(C_A)^{1/2}$, then the point is flagged for further analysis. Since the duration of a flare can be very short (see, e.g., Robinson et al. 1995), it is important that such events be contained within a single time bin if possible. For this reason, each binning interval was sampled at all possible phases, and the maximum intensity at each observation time was selected. To illustrate this technique, assume that we are binning the time sequence into 3 s intervals and that the flare starts 200 s into the time sequence and lasts for 3 s. A normal binning process, starting at time step 1, would combine times 198, 199, and 200 in one bin and 201, 202, 203 into another. Thus, the signal from the burst is split between two bins and diluted, perhaps below a detectable level. By also examining time sequences that start at time steps 2 and 3, we produce a bin that combines times 200, 201, and 202, which would presumably contain the largest signal and thus be selected in the analysis.

At each selected point we then calculated the probability that the observed number of counts in that time bin could arise from a Poisson distribution that peaks at the observed average count for that time interval. The inverse of this probability is then taken as the level of significance. In this way we build up a data set that isolates the times of significant flux increases. The results are illustrated in Figure 5, which shows examples of several types of bursts. The burst at 360 s is relatively simple and is characteristic of most of the small events in our sample. At small binning factors only the peak of the event is strong enough to become detectable. At larger binning factors the weaker emission at the start and end of the burst becomes visible, allowing us to get a lower limit to the event duration and some idea of the shape of the burst. While many of the events show a somewhat slower decay time than rise time, as normally seen for optical flares (see, e.g., Haisch, Strong, & Rodono 1991), the majority of the simple events were similar to those shown in Figure 5 and have a nearly symmetrical appearance. The larger flare events often appeared to be groups of bursts, as illustrated by the event starting at $\sim$600 s in Figure 5. This trend becomes more dominate as the size of the event increases and is the case for all four of the large, easily seen flares in Figure 1.

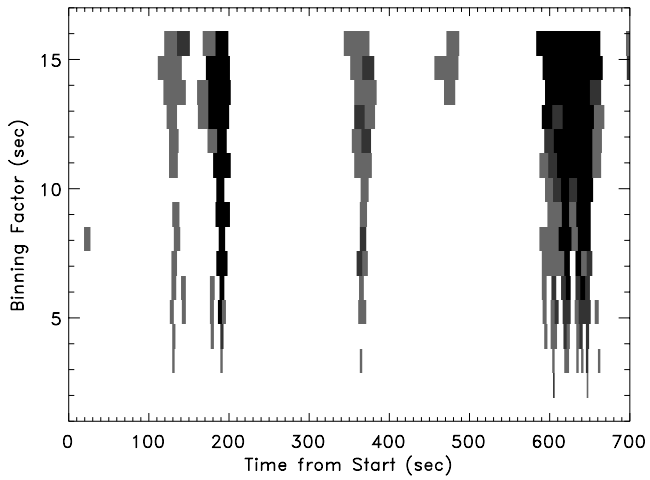


FIG. 5.—Samples within the wavelength-integrated C IV time sequence that deviate from the background by a significant amount, as a function of the temporal binning factor. The data represent the first part of orbit 1. Samples marked in light gray have a chance of less than 1 in 10^3 of being caused by background noise. Dark gray points have a chance between 1 in 10^3 and 1 in 10^4, while black points have a chance of less than 1 in 10^5.

Having objectively identified the times of the flare events, we then determined their integrated fluxes and occurrence rates. While the threshold for detectability was only 2 σ in the initial analysis, all of the events selected for the final analysis were required to exceed that threshold in at least two consecutive bins. This reduced the probability that a noise feature is inadvertently classified as a flare, but reduced the completeness of detection for the very low-intensity events.

As mentioned earlier, the longer duration flares showed the greatest enhancements in the continuum and the C IV and Si IV emission lines. This proved to be the case for the smaller events as well. During the 10,105 s of observation, we observed 32 well-defined continuum bursts, 49 events at Si IV, and 51 at C IV. In identifying these events it was occasionally difficult to separate a single burst from a nearby group of bursts, which was identified as a single large event. We therefore adopted a selection criterion such that a burst was considered to be a separate event if there was a period of at least 20 s on either side of the event when the flux was not significantly stronger than the background.

In Figure 6 we show the occurrence rate for events observed in the continuum and in the integrated C IV lines. In this figure we plot the number of events per hour, N, that have an integrated count (C) that is greater than the lower threshold (C_0). The Si IV flares show a very similar distribution to that shown for the C IV line. In all cases there is a rough power-law decrease, such that

$$N(C > C_0) \propto C_0^{-\alpha}, \quad (1)$$

where α is 0.85, 1.1, and 1.20 for the continuum, C IV, and Si IV, respectively. Note however, that the low-energy events

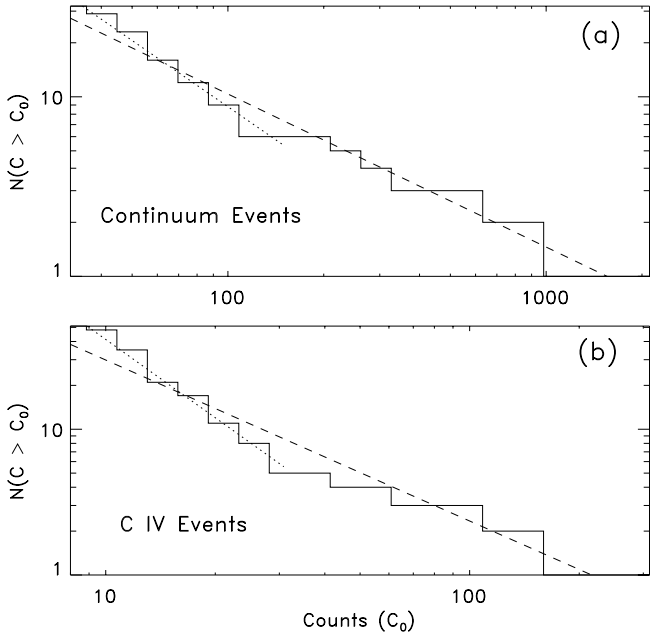


FIG. 6.—The number of flare events with wavelength-integrated counts greater than a given value (C_0) as a function of C_0. (*a*) Events detected in the continuum; (*b*) flares detected in the C IV lines. The dashed lines indicate the least-squared power law fitted to the entire data set, while the dotted line is a fit to the simple, low-energy bursts.

appear to follow a steeper slope than the higher energy events, with a break occurring at about 150 counts for the continuum and about 35 counts for C IV. Restricting the fit to energies above and below this deflection point yields $\alpha = 1.2$, 1.8, and 1.3 for the continuum, C IV, and Si IV fluxes, respectively, of the low-energy flares and 0.5, 0.6, and 0.55 for the high-energy events.

3.2. *Flare Dynamics*

It is evident from Figures 2 and 4 that the time history of the flares as seen in the continuum and various lines can be somewhat different, reflecting the complex nature of the events. The simple bursts described in § 3.1, however, may provide a much simpler physical situation in which to study the basic properties of the event. Unfortunately, since these events were weak, the flux enhancements were often seen in only one of the time sequences.

To identify events seen in two or more spectral diagnostics, we plotted the start and end time for each of the events detected in the continuum, C IV, and Si IV time histories. Flux enhancements were judged to originate from the same flare event if the times overlapped at any point. In this way we identified five events with both continuum and C IV but no Si IV, 14 bursts seen in the continuum and Si IV but not C IV, 12 events seen in C IV and Si IV but not in the continuum, and 12 bursts detected in all three diagnostics. In Figure 7 we plot the flux-flux relations for all events with overlapping detections. The error bars are determined by assuming Poisson counting statistics. The continuum versus Si IV relation is very similar to the continuum versus C IV plot and is not shown. The integrated counts in this figure can be converted to fluxes (in ergs cm^{-2}) using the conversion factors 5×10^{-14}, 4×10^{-14}, and 2.8×10^{-14} (ergs cm^{-2}) $count^{-1}$ for the continuum, C IV, and Si IV, respectively. Thus a typical microflare with 10 counts in the lines and 40

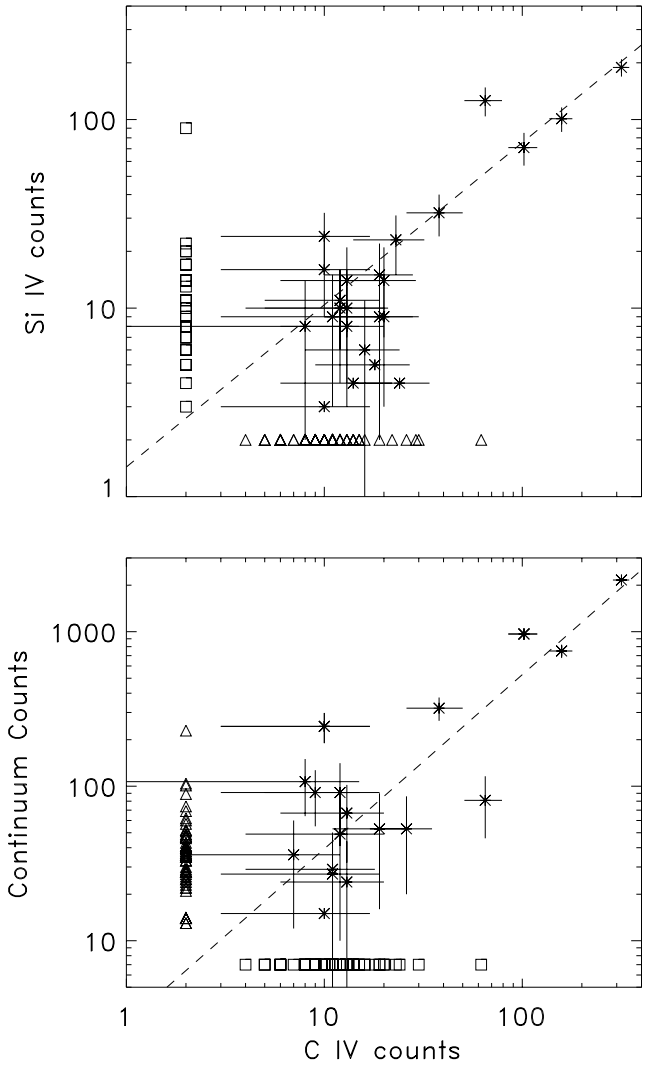


FIG. 7.—Relation between the counts detected in the Si IV lines (*top*) and the continuum (*bottom*) as a function of the counts in the C IV lines. Crosses represent flares detected in both diagnostics. The error bars are calculated from the total number of counts assuming Poisson statistics. Squares represent events seen in only one diagnostic. The dashed line is the least-square fit to a power-law distribution using only those points detected in both diagnostics.

counts in the continuum would release an energy of $\sim 2 \times 10^{28}$ ergs in the continuum and $(4–5) \times 10^{27}$ ergs in each of the lines (assuming a distance of 10 pc to AU Mic; see Paper I).

There appears to be a significant correlation between the individual fluxes for the larger events, although a few events clearly deviate from this trend. For example, one event has a flux of nearly 60 counts in C IV (more than 10 times the detection limit) with no indication of excess emission in either Si IV or the continuum. This relation appears to break down completely for the smaller, isolated bursts. Thus, for example, continuum bursts with fluxes ranging from 15 to 250 counts and Si IV events with fluxes from 4 to 20 counts were associated with C IV events having only 10 counts.

Since the continuum and line fluxes are expected to originate in different temperature regimes, the relative timing of associated bursts should provide information about the dynamics of the event. In Figure 8 we show the difference in start times for associated events. Here we have restricted

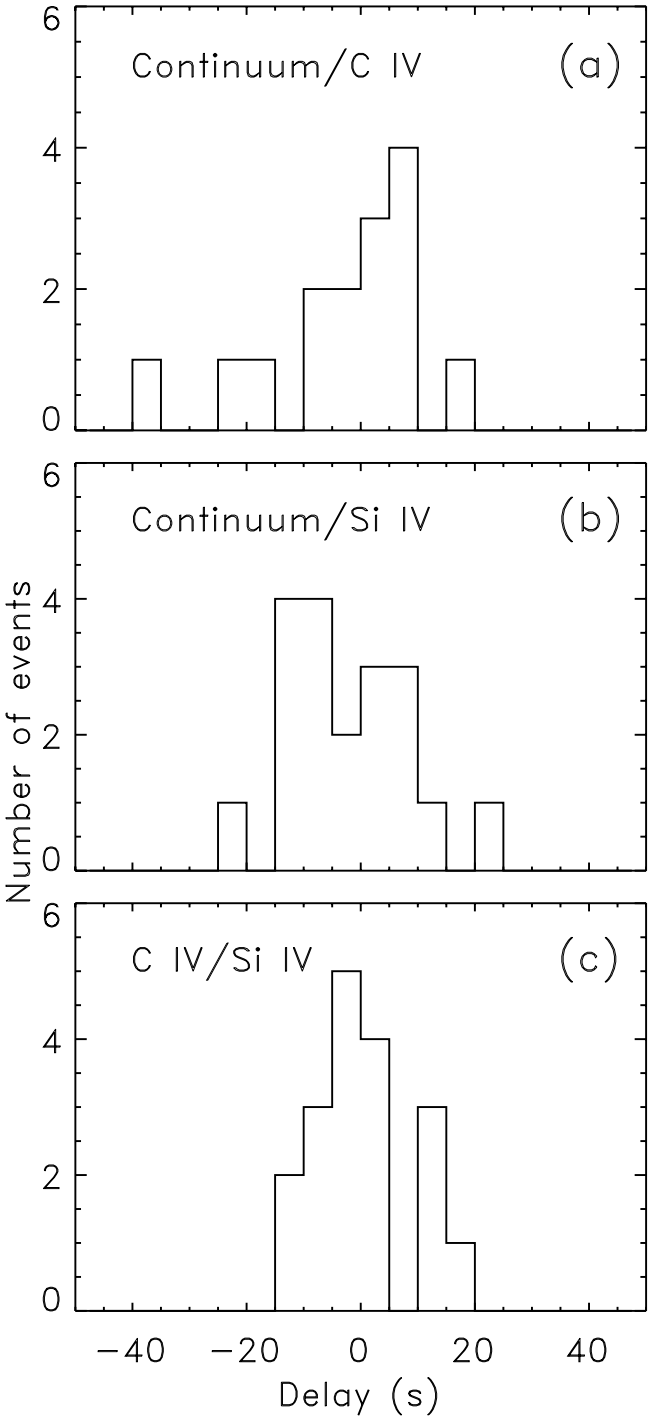


FIG. 8.—(*a*) Time delay between the onset of a flare in the continuum and the onset in the C IV emission line. (*b*) Delay between the continuum and the Si IV emission . (*c*) Delay between the C IV and Si IV start times.

ourselves to simple bursts, since these are presumably associated with a single initiating event. If the events detected in the separate time series were unrelated, then we might expect a fairly uniform distribution over an average lifetime of a burst (since we required that associated bursts overlap in time). Clearly, the Si IV and C IV events (Fig. 8*c*) are closely related, with a pronounced peak near the zero time shift. There is a much looser relation between the start times of the continuum and the line fluxes. As seen in Figures 8*a* and 8*b*, the continuum can precede as well as follow the line emission. This is not consistent with what would be expected if the event were initiated high in the atmosphere (creating the line emission) and propagated down to regions where a bound-free continuum was formed. However, it is compatible with a continuum formed primarily by a blending of numerous weak emission lines, as discussed in § 4.3.

As shown in Figure 9, the simple bursts are relatively short-lived, with lifetimes down to the detection threshold of about 5 s. As might be expected, the stronger bursts tend to have the longest durations (Fig. 10). Note that the Si IV fluxes are roughly proportional to the event duration over the entire range of observed intensities. The C IV and short-duration continuum bursts exhibit the same behavior. The longer duration continuum events, however, seem to show a dramatically different behavior, increasing in flux almost as the square of the duration.

One of the persistent questions about flares is the existence of bulk flows, since these relate directly to the energy transport process and the response of the atmosphere to the flare heating. To investigate this question we have examined the temporal variations of the C IV λ1548 line profile. Using the "quiescent" spectrum (Paper I) as a reference to define the center of the line, we determined the integrated fluxes on the red (F_R) and blue (F_B) sides of the line as a function of time and used these to define an asymmetry index, γ, as

$$\gamma = 2(F_R - F_B)/(F_R + F_B) . \quad (2)$$

A time history of γ for 20 s bins during the first *HST* orbit is presented in Figure 11, which also shows the C IV fluxes integrated over the same time intervals. The binning factor of 20 s was selected as a compromise between acceptable signal-to-noise ratio (S/N) and time resolution. The uncertainties in the value of γ were derived assuming Poisson counting statistics, as described by Robinson et al. (1999). We were surprised to find no large asymmetries during the major flare events, although there are sporadic excursions at the $\geq 2\ \sigma$ level scattered throughout the time sequence. One of the most interesting of these excursions occurs in the interval from 500 to 580 s, where there were four consecutive time intervals, each showing a significant red asymmetry. The event occurs just before the flare that starts at 590 s, but there was no flux increase at that time. A similar event appears just prior to the flare starting at 1600 s.

To better understand these asymmetries, we examined line profiles integrated over specified time intervals. The results are presented in Figure 12. Figure 12*a* shows the profile during a 5 minute "quiescent" interval, which had no apparent asymmetry changes. This is used as a reference and compares well with the quiescent profile, shown as a dotted line. Figures 12*c*, 12*d*, and 12*f* show profiles averaged over the three major flare events seen during orbit 1. These remain approximately symmetrical but show substantial broadening, suggesting enhanced turbulence or multidirectional flows. Note that this broadening varies significantly from one event to the next and is not Gaussian in character. For example, while the flare beginning at 580 s (Fig. 12*c*) shows substantial enhancements near line center, the major enhancements in the 1630 s flare (Fig. 12*f*) occur in the wings. The profiles for the preflare transients are shown in Figures 12*b* and 12*e*. In both cases there is a pronounced decrease in flux on the blue side of the profile in the velocity range between 0 and -30 km s^{-1}. Since the fluxes are decreased below those expected in the quiescent spectrum,

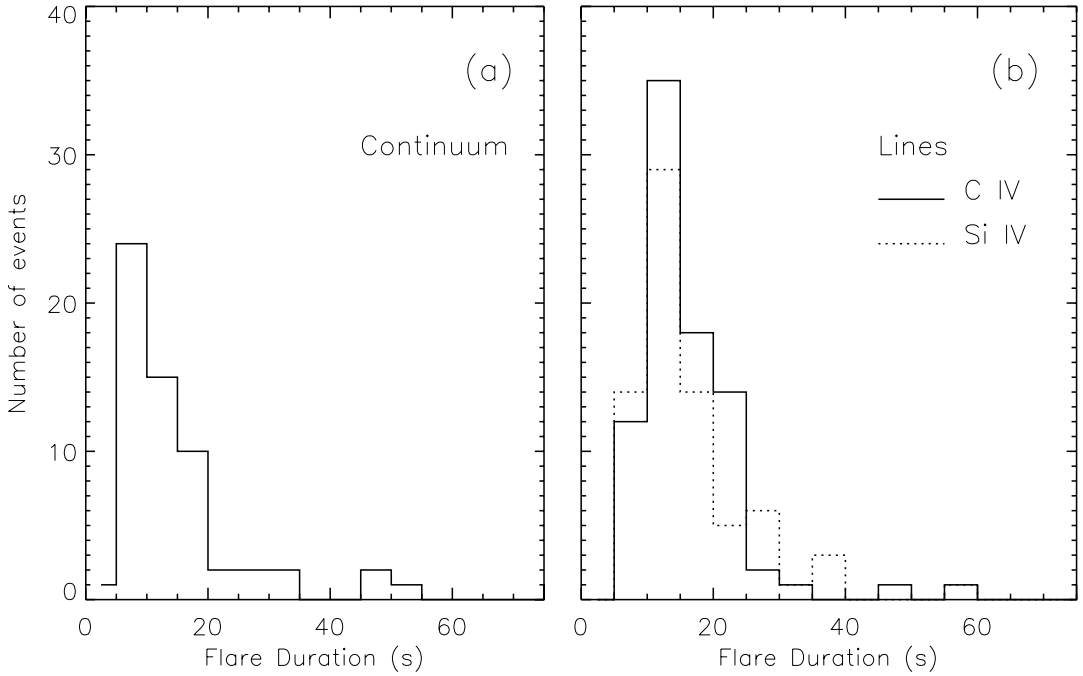


FIG. 9.—Distribution of flare durations when observed in the continuum (*a*) and the emission lines (*b*)

this suggests that a substantial absorption of the background radiation is occurring at these times.

3.3. *The Search for Proton Beams*

As first discussed by Orrall & Zirker (1976), protons accelerated toward the star during a solar or stellar flare may exchange charge with ambient hydrogen atoms and emit redshifted photons in the various hydrogen transitions, including Lyα. Thus, an enhancement in the red wing of Lyα that does not appear in the blue wing is a good indicator of the presence of proton beams. Woodgate et al. (1992) succeeded in detecting such a signal during a moderate-sized flare observed during a previous observing campaign on AU Mic. Unfortunately, the flare began before the start of the observing sequence, so the relation between the proton beam and the impulsive phase of the flare was unknown.

The signature of the proton beam detected by Woodgate et al. (1992) lasted for 3 s and contained a total of only 22 photons. Special care is therefore required in its detection. During the initial data reduction, we tabulated the observed number of counts in the blue (1207–1211.8 Å) and red (1219.5–1229 Å) wings of the Lyα line for 1 s time bins. We then used the analysis procedure described in § 3.1 to detect significant variations from the average. This is essentially the same procedure as used by Woodgate et al. (1992). We flagged an event for further study if it exceeded the average flux level by 2 σ.

During the first orbit there were three instances when the blue wing flux exceeded our detection criterion. None of these occurrences lasted more than 5 s (i.e., they were not detected in 6 s or longer time bins), and in all cases they have a significance level of less than 1:500, indicating that they could occur by chance once in 500 time samples. The other three orbits showed similar results. An analysis of the red wing fluxes shows four occasions during the first orbit in which the flux exceeded the detection threshold. In one of these cases the event was detected at binning intervals up to 15 s and had a significance level in excess of $1:10^4$, suggesting that it could be a true signature of a proton beam. This event is shown in Figure 13, which also shows the Lyα blue wing fluxes and a second, less significant enhancement. As expected, there is no variation in the blue wing during the red wind enhancement. However, comparing these plots with the observations presented in Figure 2 shows no relation between the proton beams and the times of the large flare events occurring during this orbit. This observation, however, does not necessarily imply that proton beams are not present in the larger flare events. As noted by Brosius, Robinson, & Maran (1995), an energetic proton beam can quickly ionize the ambient medium through which it propagates. This ionization substantially reduces the effectiveness of charge exchange and the red wing enhancements.

3.4. *The Presence of Coronal Plasma*

The Fe XXI line at 1353 Å is formed at temperatures near 10^7 K and was found to have the largest enhancements near the start of the first two flare events of orbit one (see Fig. 4), one starting about 20 s after the beginning of a gradual continuum and TR line enhancement and one beginning at about the same time as an impulsive increase in both continuum and line emission. There was no Fe XXI enhancement during the other two obvious flare events and only marginal increases at other times during the observations. None of these increases coincided with detected microflare bursts, and they had such low significance ($<1:1000$) and short duration (typically <5 s) that they may simply be noise. The significant bursts were also very short-lived, with lifetimes ranging from 5–20 s.

To search for long-duration coronal events similar to those often seen by the *Extreme Ultraviolet Explorer* (*EUVE*) satellite (see, e.g., Cully et al. 1993), we computed orbital flux averages of the Fe XXI line as well as the most prominent chromospheric and transition region lines. The results are given in Table 1, where the fluxes have been

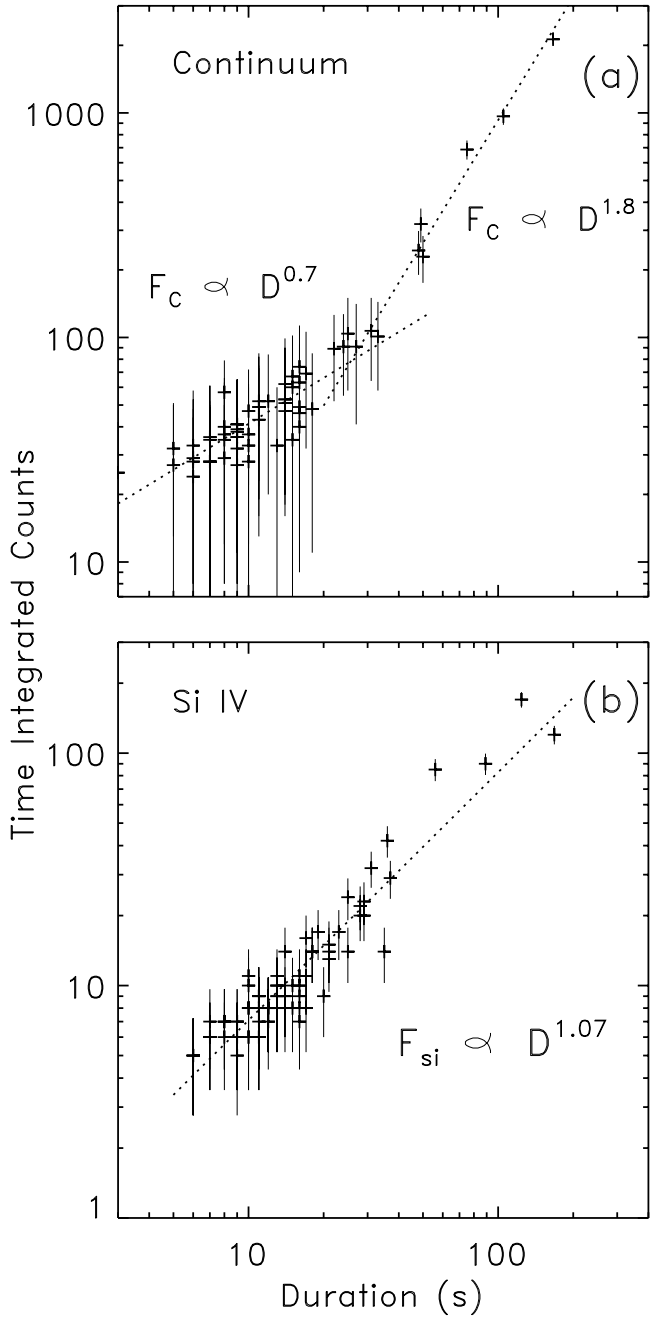


FIG. 10.—Relationship between the duration (D) and the integrated flux (in detected counts) for the continuum (a) and the Si IV lines. The vertical lines indicate 1 σ uncertainties and include uncertainties in the background. The dotted lines represent least-squared power-law fits to the observations.

normalized to their *minimum* value. Most of the chromospheric and TR lines were strongest during orbit 1, as might be expected because of the dominance of flare activity during that time. The flux in these lines then decreased during orbit 2 and remained constant (to within the flux uncertainties) for the remaining orbits. The Fe XXI line, however, was at a minimum during orbit 1 and showed a continual rise in flux, increasing by nearly 50% during the observations (about 6 hr), with the greatest enhancement occurring between orbits 3 and 4. The most plausible explanations for the rising Fe XXI flux seem to be the emergence of a bright active region from behind the limb (the star

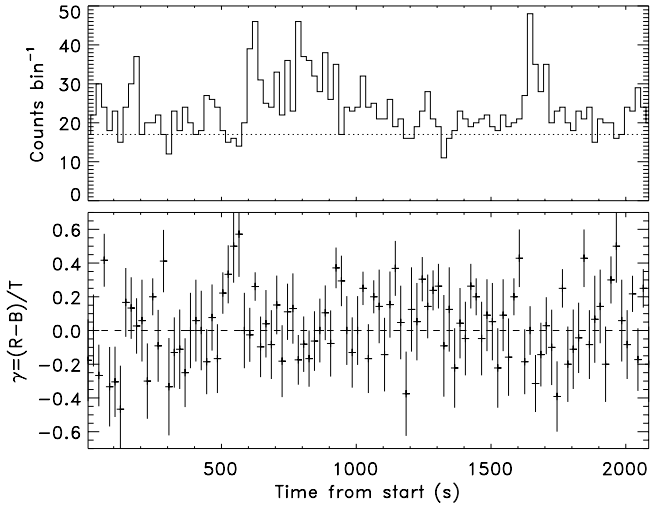


FIG. 11.—*Top*: Variation of wavelength-integrated C IV λ1548 line flux during the first orbit of observations. The samples have been binned into 20 s time intervals. *Bottom*: Measure of asymmetry for the C IV λ1548 line derived by subtracting the number of counts on the blue side of the line (B) from the number of counts on the red side (R) and dividing by the total number of counts in the line. The data have been binned into 20 s intervals and the error bars were calculated assuming Poisson statistics.

rotated $\sim 18^\circ$ during the observations) or the ejection of a plasmoid from the star (see Cully et al. 1994). However, without the full light curve for the event, it is difficult to be certain which, if either, of these possibilities is correct.

4. THE FLARE SPECTRUM

Unfortunately, the count rates are not sufficiently large to allow a detailed examination of the time history of the individual line profiles during the flares. For this reason, we integrated the data over the times of the four largest flare events (three in orbit 1 and one in orbit 2; see Figure 1) to generate an echellogram of an average flare. The scattered light was first removed from the image using the ECHELLE_SCAT routine (D. Lindler 2000, private communication) developed by the STIS Instrument Development Team (IDT), and the spectrum was extracted from the echellogram using the IDT version of the CALSTIS procedure. In the following sections this spectrum will be referred to as the average flare spectrum.

4.1. *Line Profiles and Fluxes*

In Figures 14 and 15 we compare the line profiles in our average flare spectrum with the same lines in the quiescent

TABLE 1

ORBITAL-AVERAGED LINE STRENGTHS (NORMALIZED)[a]

	Line Strength			
Line	Orbit 1	Orbit 2	Orbit 3	Orbit 4
Fe XXI...	1.00 ± 0.072	1.07 ± 0.066	1.13 ± 0.068	1.46 ± 0.078
Lyα.....	1.03 ± 0.006	1.00 ± 0.005	1.00 ± 0.005	1.03 ± 0.005
O I	1.10 ± 0.020	1.00 ± 0.017	1.05 ± 0.017	1.04 ± 0.017
C II.....	1.13 ± 0.016	1.00 ± 0.014	1.03 ± 0.014	1.01 ± 0.014
Si IV	1.47 ± 0.030	1.05 ± 0.023	1.00 ± 0.022	1.05 ± 0.023
C IV	1.37 ± 0.022	1.00 ± 0.017	1.04 ± 0.017	1.07 ± 0.017
He II	1.18 ± 0.026	1.00 ± 0.021	1.03 ± 0.021	1.01 ± 0.021

[a] Tabulated uncertainties are standard deviations calculated assuming Poisson statistics.

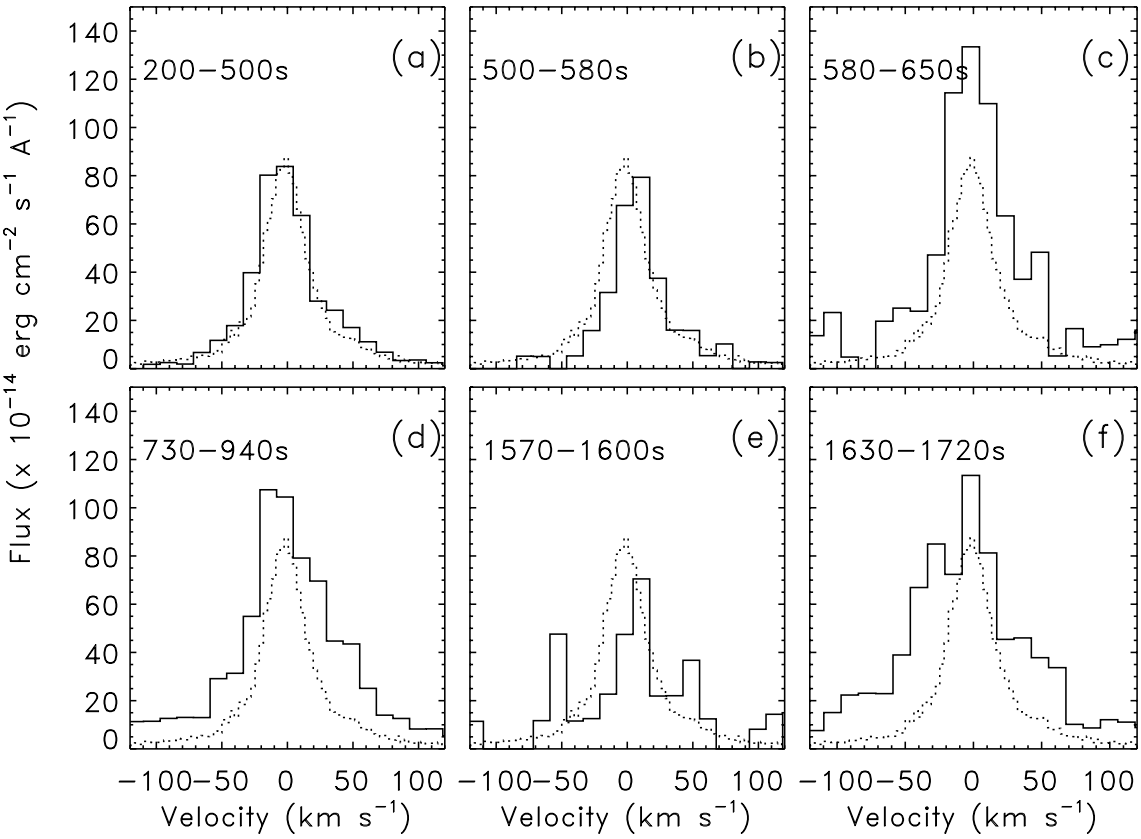


FIG. 12.—C IV λ1548 line profiles integrated over the specified times during the first orbit of observations (*solid histogram*). The dotted line is the quiescent profile obtained from a 9200 s exposure.

spectrum discussed in Paper I. This spectrum was derived from the same data set used in the present paper, except that it represents an integration over all times outside of the four major flare events. From Figure 14 it is obvious that the Lyα line shows no noticeable change during the flare, confirming the results of the time history analysis in § 3. The C III (UV4) lines, which are good density diagnostics, do show a substantial variation, especially in the relative line strength. This implies a significant change in transition region density, which will be discussed in more detail in § 4.4. Perhaps the most dramatic changes occurred in the Si IV (UV1) and C IV (UV1) lines (Fig. 15), which show substantial increases in width during the flares.

To examine the flare properties quantitatively, we assume that the flare covers only a small fraction of the stellar surface (see, e.g., van den Oord et al. 1996). If this is true, then our quiescent spectrum is a reasonable representation

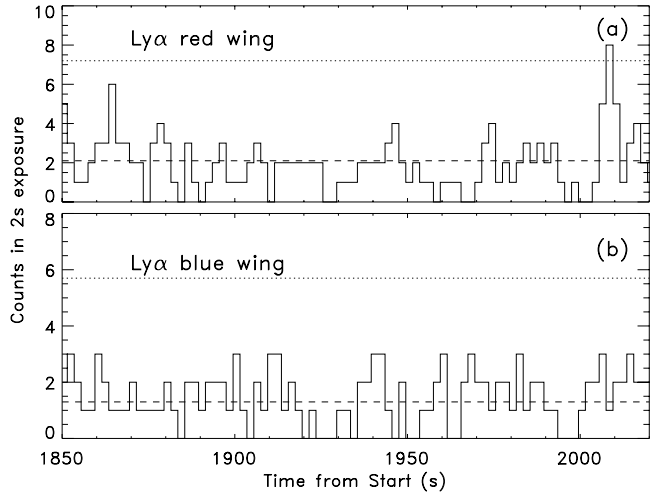


FIG. 13.—Time history of the observed counts in the red (*a*) and blue (*b*) wings of the Lyα profile. The data have been binned into 2 s intervals to improve the S/N characteristics. The dashed lines indicate the average counts per bin, while the dotted lines show the 3 σ detection threshold.

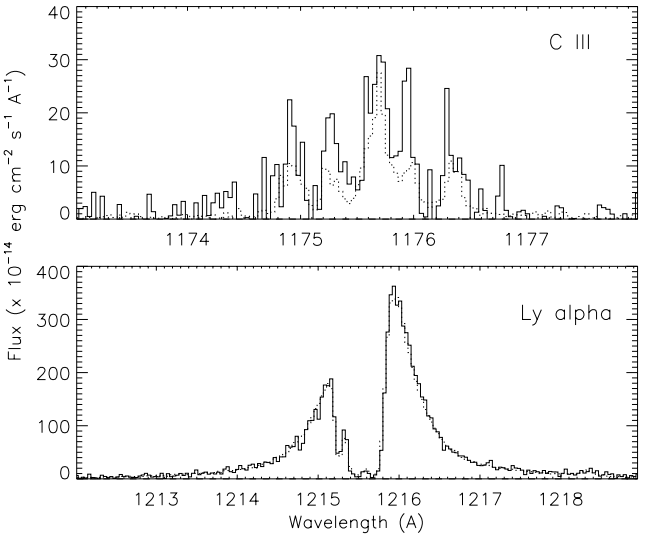


FIG. 14.—Comparison of line profiles from a time-averaged flare (*solid histogram*) and the star in quiescence (*dotted line*).

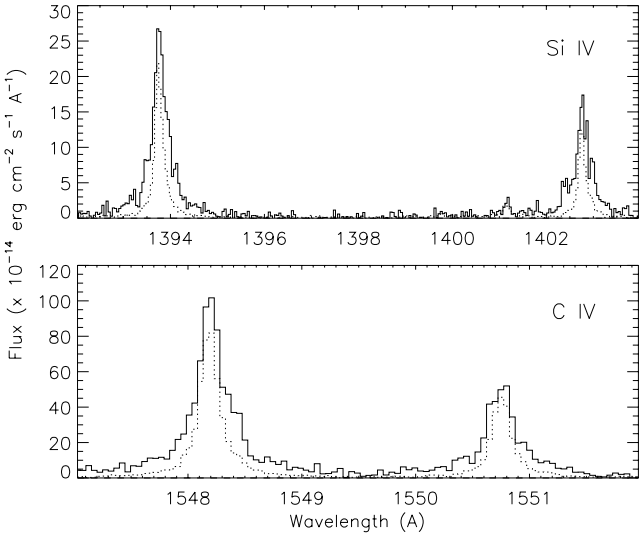


FIG. 15.—Comparison of line profiles from a time-averaged flare (*solid histogram*) and the star in quiescence (*dotted line*).

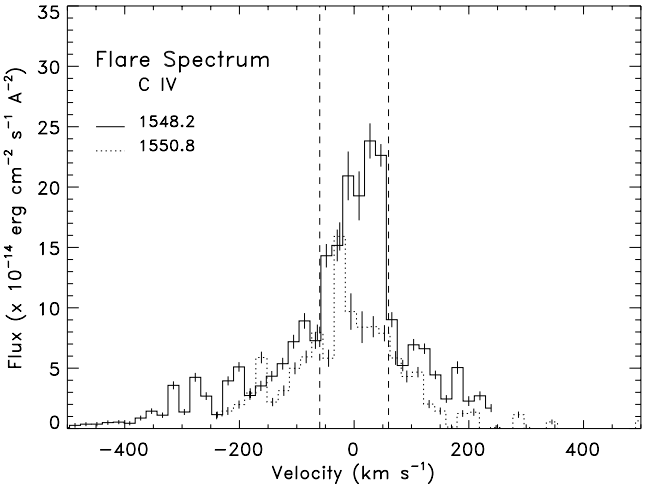


FIG. 17.—Comparison of the two C IV resonance lines. The details are the same as those in Fig. 16.

of the quiescent contribution to the observed spectrum averaged over the flare times. The pure flare spectrum is therefore derived by simply subtracting the quiescent spectrum from the observed flare spectrum. The results for the Si IV and C IV resonance lines are shown in Figures 16 and 17. Note that these profiles are non-Gaussian and contain a large amount of narrow, statistically significant fine structure, which may indicate the presence of well-defined, collimated flows. Note, however, that the overall profiles are basically symmetric. The greatest enhancements occur inside velocities of ± 60 km s^{-1}, indicating that most flare material has flows or turbulence within this velocity range. However, the Si IV lines have a substantial enhancement in the 60–90 km s^{-1} range, which is absent from the C IV line profile, showing the presence of relatively cool (i.e., 60,000 K) downflows. The enhancement of the far wings in both

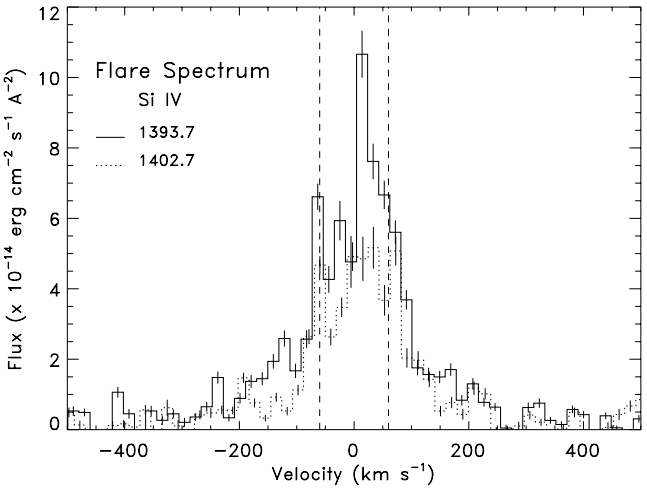


FIG. 16.—Comparison of the two Si IV resonance lines for the time-averaged flare spectrum. The spectra have had the quiescent component removed and have been wavelength binned to improve the S/N characteristics. The error bars are calculated assuming Poisson counting statistics. The vertical dashed lines are located at ± 60 km s^{-1} and are used as reference points when comparing these profiles with those in Fig. 17.

sets of lines points to the presence of turbulence with velocities of 400 km s^{-1} or more.

In the case of an optically thin, LTE atmosphere, the ratio of intensities for the strong C IV and Si IV resonance lines should equal the ratio of the *gf*-values, which is 2 in both cases. As the atmosphere becomes optically deep, this ratio approaches 1. Integrating over the line profiles shows a ratio of 2.05 ± 0.18 for Si IV and 2.02 ± 0.22 for C IV (see Table 2), indicating an optically thin plasma in both multiplets for the average flare. This is quite different from the conclusions of Mathioudakis et al. (2001), who measure wavelength-integrated Si IV line ratios of 1.17 and 1.45 and a C IV line ratio of 1.57 during two flare events on the active dMe flare star YZ CMi, implying a marginally optically thick plasma. An inspection of Figures 16 and 17 shows that the line ratios can, in fact, vary considerably across the line profile. In Figure 16, for example, the plasma moving at velocities between 0 and 50 km s^{-1} produces a Si IV intensity ratio of ~ 2, implying that it is optically thin. However, at velocities near -80, 20, and 100 km s^{-1}, the intensity ratios are about 1. A similar situation exists for the C IV profile shown in Figure 17, except that here we have the interesting situation in which the intensity ratio is greater than 2 for the velocity range 0–50 km s^{-1}. This suggests an extremely inhomogeneous source in which the two lines of the multiplet are formed in regions having very different physical characteristics.

4.2. *Average Flare Emission Measure*

In Table 2 we present the integrated, background-subtracted fluxes for all emission lines having measurable increases in the average flare spectrum. These fluxes can be used to establish an average differential emission measure (DEM) for the flare plasma, defined as $\int_V N_e N_H dV$. In general, an emission line is formed over a temperature range of $\Delta \log T_e \sim 0.3$. Thus, since an emission measure must refer to some temperature interval, we follow the formalism of Griffiths & Jordan (1998) and Paper I and calculate the parameter $\xi^{0.3}$, which is the average DEM over a temperature interval $\Delta \log T_e = 0.3$. In Figure 18 we show the function $G_{ij}(T_e) \equiv \frac{1}{2} h\nu_{ij} f$ (see eq. [5] of Paper I), which is consistent with the observed flux for each emission line

TABLE 2

SUMMARY OF EMISSION-LINE FLUXES

Line	Temperature (×1000 K)	Quiescent Flux ($\times 10^{-14}$ ergs cm^{-2} s^{-1})	Average Flare Flux[a] ($\times 10^{-14}$ ergs cm^{-2} s^{-1})
C III λ1175.0	63	13.2 ± 1.2[b]	11.0 ± 3.0[b]
Si III λ1206.5	32	7.9 ± 0.5	0.6 ± 0.3
O V] λ1218.3.....	250	1.83 ± 0.3	0.3 ± 0.25
N V λ1238.8.....	200	4.5 ± 0.5	1.2 ± 0.4
N V λ1242.8.....	200	2.1 ± 0.3	0.5 ± 0.3
O I λ1302	<10	1.9 ± 0.25	0.4 ± 0.25
O I λ1304	<10	4.9 ± 0.4	0.4 ± 0.25
O I λ1306	<10	5.0 ± 0.4	0.5 ± 0.25
C II λ1304.5	40	6.0 ± 0.5	1.6 ± 0.6
C II λ1335.7	40	16.7 ± 0.7	2.3 ± 0.6
Fe XXI λ1354.....	10000	0.77 ± 0.2	0.23 ± 0.2
O V λ1371.....	250	0.35 ± 0.1	0.23 ± 0.15
Si IV λ1393.7	63	4.93 ± 0.3	8.4 ± 0.45
Si IV λ1402.7	63	2.92 ± 0.25	4.1 ± 0.3
C IV λ1548	102	21.4 ± 1.0	21.6 ± 1.3
C IV λ1550	102	11.3 ± 0.8	10.7 ± 1.0
He II λ1640.....	80	26.4 ± 1.0[b]	1.6 ± 1.1[b]

[a] Residual fluxes after subtraction of the quiescent background.

[b] Fluxes represent an integration over the entire multiplet.

showing significant variations during the flare. This function basically defines the proportionality between the observed flux of a line and the emission measure of plasma at a specified temperature (T_e) that is required to generate that flux. The values of G_{ij} were derived from the CHIANTI database (Dere et al. 1997) and adjusted to AU Mic using the stellar distance of 9.9 pc, obtained from the Hipparcos catalog (Perryman et al. 1997). The emission from the permitted lines (C II, Si IV, C IV, and N V) is relatively insensitive to density and was determined assuming an arbitrary density of 10^{10} cm^{-3}. The emission from the O V] lines, however, is critically dependent on the density and was calculated assuming $N_e = 1.7 \times 10^{12}$ cm^{-3} (see § 4.4). At this density the required DEM agrees for the two O V] lines and is consistent with that expected from the other hot lines.

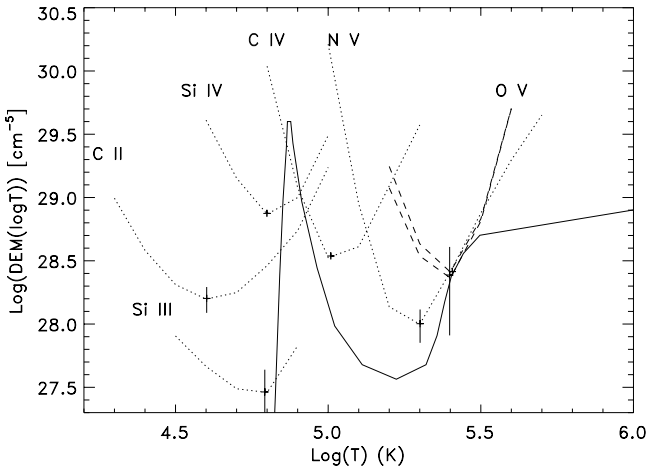


FIG. 18.—Function $G_{ij}(T_e)$ for each of the emission lines showing significant enhancements in the time-averaged flare spectrum (*dotted lines*). The vertical line at the minimum of these distributions shows the range of values allowed by the uncertainties in the flux measurements. The dashed lines are the G_{ij} functions for the O V] λλ1218 and 1371 lines assuming a density of 1.7×10^{12} cm^{-3}. The solid line is the emission measure distribution deduced from the individual line fluxes as described in the text. The steep decline at low temperatures is needed to account for the small enhancements of lower temperature lines, while the upward sloping line at high temperatures extends to the measured DEM of the Fe XXI λ1353 line.

The actual emission measure distribution was determined through an iterative procedure in which we specified a DEM distribution based on the G_{ij} functions, calculated the line fluxes, and adjusted the emission measure until the calculated and observed fluxes agree to within 10%. The results of these calculations are shown in Figure 18. The general trends of the G_{ij} functions suggest that the DEM goes through a peak near a temperature of 85,000 K. During the analysis it was found that this peak is extremely sharp, reaching a value of $\sim 4 \times 10^{29}$ cm^{-5} at 80,000 K and having a width of only about $\Delta \log T_e = 0.1$. The DEM must drop off sharply at temperatures below 55,000 K to account for the small enhancements in the O I, C I, and C II lines. Thus most of the observed C II flux probably comes from plasma near the peak of the DEM distribution, well away from the optimum temperature of formation for this line. At higher temperatures the DEM reaches a minimum near 1.2×10^5 K and then begins increasing again, reaching a value of 3×10^{29} cm^{-5} near 10^7 K (deduced from the Fe XXI emission). This behavior suggests that we are dealing with separate high- and low-temperature components of the flare, possibly associated with the energy release (impulsive) and relaxation (thermal) phases, respectively. This idea is supported by the fact that emission from the hot plasma is primarily observed during the initial phases of the largest flare events in the sample (see § 3.4).

While the DEM distribution presented in Figure 18 accounts for the observed enhancements of most of the lines, we were unable to find any solution that accounted for the relatively small increase seen in Si III λ1206. Emission from this line has a very similar temperature dependence to the Si IV (UV1) multiplet and is expected to have an integrated flux that is comparable to the combined fluxes of these Si IV lines. This, in fact, is what is observed in the quiescent spectrum. During the flares, however, the enhancement in the Si IV lines was more than 20 times that observed in Si III. Apparently, there are non-LTE effects

associated with the rapid drop in DEM at temperatures below 80,000 K that substantially affect the ionization of Si during the flares.

4.3. *Continuum Characteristics*

At optical and near-UV wavelengths the continuum enhancement during flares is dramatically larger at blue wavelengths than in the red. This is commonly interpreted as evidence that the continuum is formed by thermal processes in a region of enhanced temperature. To see whether such behavior occurs in the FUV, we divided the observed spectrum into two regions, one covering the wavelength range from 1150–1470 Å and the other the region 1470–1720 Å, and monitored the continuum flux within each region. In Figure 19 we plot the ratio of blue to red continuum fluxes compared with the total continuum emission, which shows the flare enhancements. The flux ratio has been binned into 10 s increments to improve the S/N characteristics. There are no obvious changes in the ratio during the flares, implying that the FUV flux increases monotonically throughout this wavelength range.

To further study the continuum properties, we identified a sequence of 10–15 Å wide spectral regions that were free of obvious emission features. We then determined the average flux in each of these regions in both the quiescent spectrum and the average flare spectrum described in § 4. The results are presented in Figure 20, where we have subtracted the quiescent component from the average flare spectrum. The flux has a jagged appearance, quite different from smooth variations expected from a true continuum emission process. These variations are much larger than expected from measurement uncertainties and have a similar shape in the quiescent and pure flare spectrum, suggesting that flare emission is basically a scaled version of the quiescent spectrum. Note, however, that there are certain wavelengths (notably near 1330, 1380, 1560, 1650, and 1680 Å) where the flare enhancements are zero. This seems to preclude the presence of a true continuum enhancement during the flare and suggests that the "continuum" increase is actually caused by the enhancement of numerous weak emission lines.

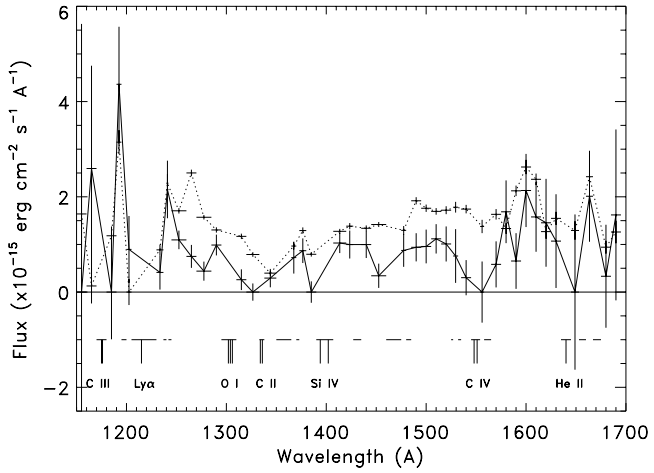


FIG. 20.—Average flux vs. wavelength for the time-averaged flare spectrum (*solid line*) and the quiescent spectrum (*dotted line*). The flare spectrum has had the quiescent component removed. The regions selected are intended to sample the stellar continuum and are free of the emission lines cataloged by Pagano et al. (2000). The vertical line indicates the flux uncertainty, based on Poisson statistics, while the horizontal line indicates the wavelength range over which the average is taken. The horizontal bars at a flux of -1×10^{-15} indicate the wavelength ranges excluded from the averaging because of observed emission lines. The location of the most pronounced emission lines are labeled.

To investigate this question we first binned the average flare and quiescent spectra to a resolution of 4600 to improve the S/N characteristics and then selected those wavelengths that excluded the 142 obvious emission lines identified in Paper I. We then plotted the histogram of the flux distribution present in each spectrum. The results are presented in Figure 21. A relatively flat continuum will appear as a Gaussian distribution centered at the average

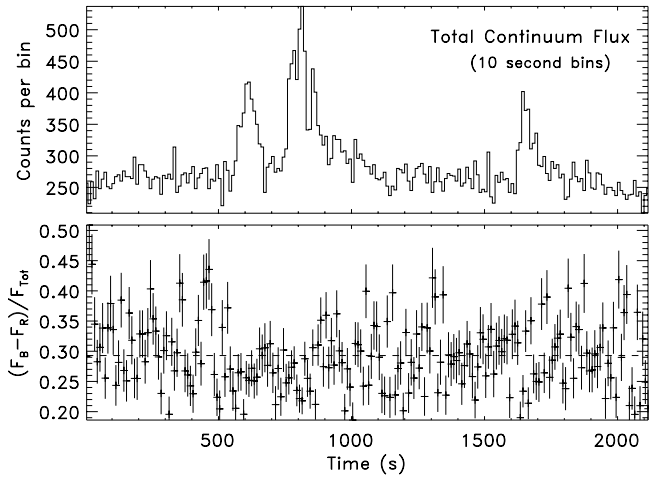


FIG. 19.—*Top*: Variation in the number of counts detected in the wavelength-integrated continuum, binned into 10 s samples. *Bottom*: Color of the continuum calculated by subtracting the number of continuum counts within the 1470–1720 Å range (R) from the number of counts in the 1150–1470 Å range and then dividing by the total number of continuum counts. Error bars are calculated assuming Poisson statistics and the dashed line shows the color value in the quiescent spectrum.

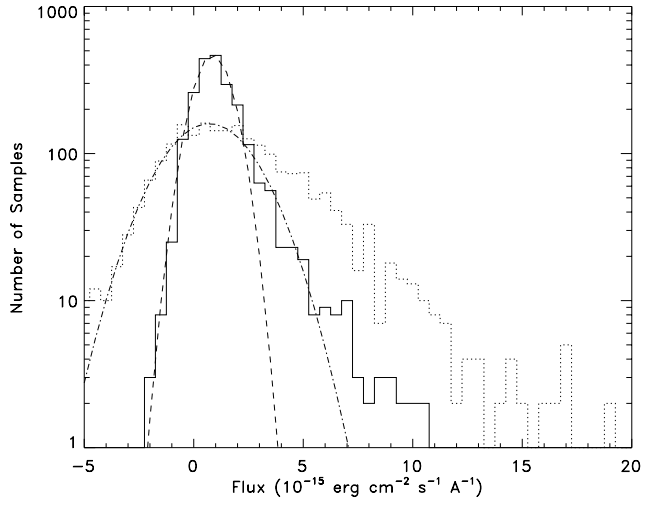


FIG. 21.—Distribution of intensities for sample wavelength points between 1250 and 1700 Å that are unaffected by pronounced emission lines. The solid line is the distribution in the quiescent spectrum, and the dotted line was taken from the time-averaged flare spectrum (which includes the quiescent component). The wavelengths have been binned to a resolution ($\Delta\lambda/\lambda$) of 4600 to improve the S/N characteristics. The dashed line is a Gaussian fit to the lower flux samples of the quiescent spectrum, while the dot-dashed line is a Gaussian fit to the flare distribution.

flux, with a width determined by the statistical noise. Weak emission lines will show up as an asymmetry toward higher fluxes. This is the situation found in Figure 21. Out of a total of 2200 wavelength samples, 2000 points in the quiescent spectrum were contained within the Gaussian distribution that was centered at a flux of $(8.5 \pm 0.7) \times 10^{-16}$ ergs cm^{-2} s^{-1} Å^{-1}. If there was a true increase in the continuum during the flares, then we would expect that the number of points within the Gaussian distribution would remain roughly constant but that the centroid would shift to higher energies. In fact, the flare spectrum contained only 1600 samples within the Gaussian, which was centered at a flux of $(7.3 \pm 0.8) \times 10^{-16}$ ergs cm^{-2} s^{-1} Å^{-1}. The larger width of the fitted Gaussian for the flare distribution is mainly the result of the shorter overall exposure time, which leads to a larger statistical noise. The increased wavelength-integrated flux during the flare, which was 1.5 times that of the quiescent spectrum, was entirely due to an enhancement of the high-energy tail of the distribution, which we assume is caused by the strengthening of numerous weak emission lines.

4.4. *Flare Densities and Sizes*

Flare-related emission was only detected in two major density diagnostics: the O v] line at 1218 Å combined with the O v λ1371 line and the C III multiplet near 1175 Å. For densities less than 10^{10} cm^{-3}, the O v] emission at 1218 Å is expected to have nearly 20 times the intensity of the λ1371 line. As the density increases, the relative strength of the λ1371 line also increases, reaching the same level as the λ1218 line for $N_e \sim 2 \times 10^{12}$ cm^{-3}, as shown in Figure 22 (from the CHIANTI database). As seen from Table 2, the strengths of the two O v lines were comparable in the background-subtracted flare spectrum, with an intensity ratio of $R(1371/1218) = 0.76 \pm 0.6$. This ratio indicates densities ranging from 3×10^{11} to 3×10^{12} cm^{-3}, with the most probable density (from the measured ratio) of 1.7×10^{12} cm^{-3}. This is comparable to the high-density component of the quiescent emission of AU Mic (Paper I), which was attributed to microflare radiation. The density is also the value required for the volume emission measure (VEM) of the O IV lines to agree with that derived from the permitted N v lines formed at a similar temperature (see § 4.2).

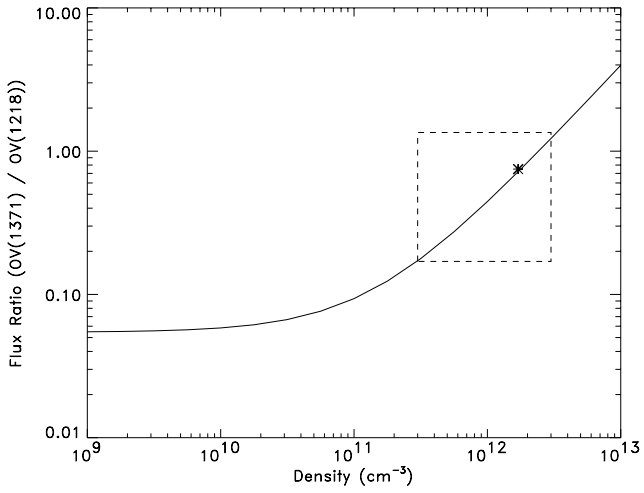


FIG. 22.—Density vs. line ratio relationship for the O v] λ1218 and O v λ1371 lines. The dashed box indicates the range of possible densities given the observed ratio and its uncertainties. The asterisk indicates the most probable density.

An estimate of the flare size can be obtained from this density estimate combined with the volume emission measure ($\sim N_e^2 V = 1.7 \times 10^{50}$ cm^{-3}) for the O v lines (see Fig. 18). Assuming a cylindrical shape of height 100 km, which is a typical density scale length near these densities (Hawley & Fisher 1992), we find an area of $\sim 6 \times 10^{18}$ cm^2 for the average flare, which is about 0.1% of the stellar surface. This can be compared with the fractional surface area of 4.5% that Hawley et al. (1995) infer from a giant flare observed on this star by the *EUVE* satellite.

A rough idea of the density associated with the hot coronal plasma can be obtained from the observed decay time of the Fe XXI bursts using two separate techniques. First, if the flare decay time is small compared to that expected for conduction, then we can assume purely radiative losses. The radiative loss rate per unit volume for an optically thin source can be expressed by the function $P(T)$ (Landini & Monsignori Fossi 1990), which is the radiative loss rate per unit emission measure at temperature T. The thermal energy per unit volume for a plasma is $N_e kT$. We can therefore define a radiative decay time ,$\tau_{\rm rad}$, as the total energy per unit volume divided by the radiative loss rate, or

$$\tau_{\rm rad} = \frac{kT}{P(T)N_e} . \tag{3}$$

This expression can then be solved for N_e in terms of an observed value of $\tau_{\rm rad}$. Landini & Monsignori Fossi (1990) give a value of $P = 2.5 \times 10^{-23}$ ergs cm^{-3} s^{-1} for a plasma at 10^7 K. Assuming a $1/e$ decay time of 10 s for the events seen in the Fe XXI line (which is probably an overestimate), this gives a density of $\sim 6 \times 10^{12}$ cm^{-3}, which is comparable to the values deduced from density-sensitive lines in the *EUVE* spectra of flares on AU Mic (see, e.g., Monsignori Fossi et al. 1996). Note, however, that somewhat higher densities would be implied if there were continued heating during the event.

A second method of estimating density is based on the sudden heating of the atmosphere by the flare, which creates a large pressure imbalance and a consequent outward expansion of the source at near the local sound speed [$v_e = (2kT/M_p)^{1/2}$; see, e.g., Katsova, Boiko, & Livshits 1997], about 400 km s^{-1} for a plasma at a temperature of 10^7 K. Assuming that the source is represented by a single temperature, then the amount of flux radiated by the source at time t, $\Phi(t)$, is simply given by $\Phi(t) = P(T)N_e^2 V(t)$. If we assume that the total number of hot particles ($N_T = N_e V$) is a constant (i.e., there is no continued heating), then the radiated flux can be expressed as

$$\frac{\Phi(t)}{\Phi(0)} = \frac{P(T)}{P(T_0)} \frac{V(0)}{V(t)} \approx \frac{V(0)}{V(t)} , \tag{4}$$

since $P(T)$ changes very slowly with temperature near 10^7 K. The most rapid flux decrease occurs when the source expands spherically, so that $V(t) \propto [1 + (v_e t/l_0)]^3$, where l_0 is the initial length scale of the heated region. The slowest decrease occurs when the expansion is in one dimension, as would be the case if magnetic fields restricted the lateral expansion of the source. In this case $V(t) \propto [1 + (v_e t/l_0)]$, and l_0 refers only to the height of the source region. Using these expressions in equation (4) and defining a flux decay time, $\tau_{\rm exp}$, as that time for which $\Phi(\tau_{\rm exp})/\Phi(0) = 0.1$, we can

obtain a relation between l_0 and τ_{exp}. Assuming $\tau_{exp} = 10$ s, we find that $l_0 = 4000$ km for the spherically expanding source and 450 km for a linear expansion.

To obtain the density of the hot plasma, we use the observed VEM to obtain a further constraint on the density and volume. Near the peak of the Fe XXI burst the count rate in the line was measured to be 0.45 counts s^{-1}, which translates to a flux of 1.3×10^{-14} ergs cm^{-2} s^{-1} and a VEM of 5×10^{50} cm^{-3} at a temperature of 10^7 K. Combining this with the length scale of 4000 km for the spherically expanding hot plasma gives a density of 1.5×10^{12} cm^{-3}, which should be viewed as a lower limit. For a linearly expanding cylindrical source of cross-sectional area A, the volume can be expressed as $V = Al_0 = \pi\eta^2 l_0^3$, where η is the width-to-height ratio of the cylinder. Under this approximation and using the value of $l_0 = 450$ km, we obtain the estimate $N_e \sim 4.5 \times 10^{13}/\eta^2$ cm^{-3}. If $\eta \sim 1$, this implies a density somewhat larger than that estimated from radiative losses. This is unlikely, since in that case the flux would decrease before a significant expansion would occur. Thus η is probably larger than 1.

5. DISCUSSION AND CONCLUSIONS

In this second paper on AU Mic we report on the analysis of 10,105 s of FUV spectroscopic observations of this dM4.5e flare star. During this time we detected 43 flare events, covering a factor of more than 30 in integrated flux. In most cases these were single bursts, ranging in duration from $\sim$5 to 20 s. These flares show a rapid increase and decay in flux, with very little indication of an extended thermal phase. The larger events are composed of groups of bursts, in agreement with the UV photometry presented by Robinson et al. (1995, 1999). As expected from ground-based optical observations (e.g., Gershberg & Shakhovskaya 1983; Haisch et al. 1991), the flares are consistent with a power-law distribution between flare-occurrence rate and time-integrated flux. At high energies the slope (α) of this power law is comparable to that found for optical flares, which is typically around 0.8 ± 0.3 (Gershberg & Shakhovskaya 1983). At low energies, however, the slope is considerably larger than 1, which is significant because it shows that the low-energy flares (microflares) may play a role in heating the chromosphere (see, e.g., Hudson 1991).

The flares were most apparent in the integrated continuum and in the lines of Si IV and C IV. A detailed examination of the time sequences showed that the relative behavior of these diagnostics was quite complicated. On average, the Si IV and C IV lines showed similar enhancements. This is what might be expected, since the lines are formed at similar temperatures. There were instances, however, when there were large discrepancies in their relative fluxes, such that a highly significant event was seen in one multiplet but no indication of the burst in the second. This suggests that the flare heating can produce emission only in a remarkably narrow range of temperatures. Further, while bursts seen in both multiplets tended to peak at the same time on average, there were several cases where the start time of one is displaced by as much as ± 20 s from that of the other. While such delays may be interpreted as propagation effects, we suspect that we are actually seeing two separate, though related, events. Similar characteristics are seen in the relations between the continuum and line enhancements, where the start of the continuum burst was seen to both lead and follow the start of the line enhancements. This behavior is contrary to the expectations of most solar flare models (e.g., Shibata et al. 1995; Katsova et al. 1997), in which the initial energy release occurs high in the atmosphere and propagates downward, first heating the transition region (lines) and then the chromosphere and temperature minimum region (continuum). However, this behavior may occur if the magnetic instabilities (reconnection events) responsible for the flare occur in the transition region or upper chromosphere, as previously suggested by Linsky & Wood (1994) and Wood, Linsky, & Ayres (1997). The similarity in the time profiles for the flares seen in the continuum and the emission lines is also compatible with a continuum that is composed primarily of weak, blended emission lines (see below).

The short-term enhancements of the Fe XXI line at the start of the flares and the relatively large densities of the 10^7 K plasma at these times are consistent with the standard models involving impulsive heating and evaporation (e.g., Katsova et al. 1997). Unfortunately, the Fe XXI flux during these events was too weak to search for the large blueshifts observed during solar flares (see, e.g., Antonucci et al. 1993) and expected from the stellar flare models.

A crude examination of the temporal variations of the C IV line profile shows no indication of large, unidirectional flows during any portion of the major flare events. An examination of the line profiles integrated over each of the major flares, however, does show a significant broadening. Thus, bulk flows and turbulence do, in fact, increase dramatically during the events, but no preferred direction is seen in our data, unlike the downflows observed by Bookbinder et al. (1992) during a flare on AD Leo. While most of the observed velocities occur in the range of ± 60 km s^{-1}, enhancements at velocities as large as ± 200 km s^{-1} were seen. This broadening is comparable to the extent of the wings of the strong resonance lines in the quiescent spectrum of AU Mic , which Paper I suggests are the result of nanoflares. Note, however, that the power in the high-velocity flare component is relatively small compared to that in the low velocities. Thus, if nanoflare emission is indeed the cause of these broad resonance line wings, then these events must have a much larger fraction of their emission at high velocities than is the case for the larger bursts.

One surprising result is that the enhanced emission during the flares was most apparent in the intermediate-temperature Si IV and C IV resonance lines compared with much smaller enhancements seen in both the cooler (e.g., C II) and hotter (N V) lines. This leads to an emission measure distribution that is sharply peaked at temperatures near 10^5 K. The very restricted heating of the flare plasma is further suggested by the pronounced enhancement of the Si IV line profile in the time-averaged flare spectrum, which was seen at a velocity near 75 km s^{-1}. The C IV line showed no enhancement at this velocity. Unfortunately, we do not have contemporaneous optical spectroscopy, so we do not know whether these flares were visible in either the optical continuum or the Balmer lines.

Another surprise involved the behavior of the continuum. While there is undoubtedly a true FUV continuum associated with the quiescent emission, with a strength of roughly 8×10^{-16} ergs cm^{-2} s^{-1} $Å^{-1}$, there is no indication of such a continuum associated with the flares. For example, a true continuum is expected to have a color dependence, such that the emission at one end of the spectral range is enhanced relative to the other. However, no such changes

were detected in any of the observed flares. One of the most persuasive arguments against a true continuum comes from the form of the intensity distribution of wavelength samples outside of regions affected by obvious emission lines. During the average flare this distribution showed only an enhancement in the high-flux tail, suggesting localized flux increases from emission lines rather than an overall flux increase that would have shifted the entire distribution to higher energies. The form of the "continuum" spectrum shown in Figure 20 also suggests the presence of many weak emission lines, since it has a very ragged appearance, and there are several wavelength regions that showed no flux increases at all during the flare. The shape of the flare spectrum is very close to that of the quiescent spectrum, suggesting that microflare emission is a large contributor to the quiescent continuum.

The situation described here is substantially different from that seen on the Sun, where the flare emission at $\lambda < 1683$ Å is thought to be due to bound-free radiation from Si I that has been excited by UV emission lines (see, e.g., Machado & Mauas 1987). Phillips, Bromage, & Doyle (1992) extended this idea to dMe flare stars and used *IUE* data to show a very good relation between average continuum enhancements near 1595 Å ($F_{\mathrm{C}\,1595}$) during stellar flares and the integrated C IV fluxes ($F_{\mathrm{C\,IV}}$), which are thought to excite the continuum:

$$\log_{10} F_{\mathrm{C}\,1595} = 1.04 \pm 0.09 \log_{10} F_{\mathrm{C\,IV}} - 2.9 \pm 2.4 , \quad (5)$$

where $F_{\mathrm{C}\,1595}$ is expressed in units of ergs cm^{-2} s^{-1} Å^{-1}. This linear relation between the continuum and C IV fluxes might also be expected if the continuum were composed of a forest of weak emission lines, as suggested above. In fact, the flux enhancements in our average flare spectrum (i.e., $F_{\mathrm{C}\,1595} \sim 5 \times 10^{-16}$ ergs and $F_{\mathrm{C\,IV}} \sim 3.2 \times 10^{-13}$ erg) and the continuum/C IV flux relations shown in Figure 7 are both consistent with this relation. While our observations of reasonably weak flares shows no evidence of a true continuum during the flare, *IUE* observations of much stronger events do show a flare continuum (see, e.g., Hawley & Pettersen 1991; van den Oord et al. 1996). It is possible, therefore, that both continuum and line emission are present in the FUV enhancements during flares.

We wish to thank the anonymous referee for several helpful suggestions. This work was supported by NASA through Guaranteed Time Observation funding to the STIS science team through grant NAG 5-5239 to the Catholic University of America and S-56500-D to the University of Colorado and NIST.

REFERENCES

Antonucci, E. 1989, Sol. Phys., 121, 31
Antonucci, E., Dodero, M.A., Martin, R., Perex, G., Reale, F., & Serio, S. 1993, ApJ, 413, 786
Bookbinder, J. A., Walter, F. M., & Brown, A. 1992, in ASP Conf. Ser. 26, Cool Stars, Stellar Systems and the Sun, ed. M. S. Giampapa & J. A. Bookbinder (San Francisco: ASP), 27
Brosius, J. W., Robinson, R. D., & Maran, S. P. 1995, ApJ, 441, 385
Byrne, P. B. 1989, Sol. Phys., 121, 61
Cully, S. L., Fisher, G., Abbott, M. J., & Siegmund, O. H. M. 1994, ApJ, 435, 449
Cully, S. L., Siegmund, O. H. M., Vedder, P. M., & Vallerga, J. V. 1993, ApJ, 414, L49
Dere, K. P., Landi, E., Monsignori Fossi, B. C., & Young, P. R. 1997, A&AS, 125, 149
Gershberg, R. E., & Shakhovskaya, N. I. 1983, Ap&SS, 95, 235
Griffiths, N. W., & Jordan, C. 1998, ApJ, 497, 883
Haisch, B., Strong, K., & Rodono, M. 1991, ARA&A, 29, 275
Hawley, S. L., & Fisher, G. H. 1992, ApJS, 78, 565
Hawley, S. L., & Pettersen, B. R. 1991, ApJ, 378, 725
Hawley, S. L., et al. 1995, ApJ, 453, 464
Houdebine, E. R., Foing, B. H., Doyle, J. G., & Rodono, M. 1993, A&A, 278, 109
Hudson, H. S. 1991, Sol. Phys., 133, 357
Katsova, M. M., Boiko, A. Ya., & Livshits, M. A. 1997, A&A, 321, 549
Landini, M., & Monsignori Fossi, B. C. 1990, A&AS, 82, 229
Linsky, J. L., Neff, J. E., Brown, A., Gross, B. D., Simon, T., Andrews, A. D., Rodono, M., & Feldman, P. A. 1989, A&A, 211, 173
Linsky, J. L., & Wood, B. E. 1994, ApJ, 430, 342
Machado, M. E., & Mauas, P. J. 1987, in Rapid Fluctuations in Solar Flares, ed. B. R. Dennis, L. E. Orwig, & A. L. Kiplinger (NASA CP-2449), 271
Mathioudakis, M., McKenny, J., Kennan, F. P., Williams, D. R., & Phillips, K. J. H. 2001, A&A, in press
Monsignori Fossi, B. C., Landini, M., Del Zanna, G., & Bowyer, S. 1996, ApJ, 466, 427
Orrall, F. Q., & Zirker, J. B. 1976, ApJ, 208, 618
Pagano, I., Linsky, J. L., Carkner, L., Robinson, R. D., Woodgate, B. E., & Timothy, G. 2000, ApJ, 532, 497 (Paper I)
Perryman, M. A. C., et al. 1997, The Hipparcos & Tycho Catalogues (ESA SP-1200; Noordwijk: ESA)
Phillips, K. J. H., Bromage, G. E., & Doyle, J. G. 1992, ApJ, 385, 731
Robinson, R. D., Carpenter, K. G., & Percival, J. W. 1999, ApJ, 516, 916
Robinson, R. D., Carpenter, K. G., Percival, J. W., & Bookbinder, J. A. 1995, ApJ, 451, 795
Robinson, R. D., Carpenter, K. G., Woodgate, B. E., & Maran, S. P. 1993, ApJ, 414, 872
Shibata, T., Masuda, S., Shimojo, M., Hara, H., Yokoyama, T., Tsuneta, S., Kosugi, T., & Ogawara, Y. 1995, ApJ, 451, L83
van den Oord, G. H. J., et al. 1996, A&A, 310, 908
Wood, B. E., Linsky, J. L., & Ayres, T. R. 1997, ApJ, 478, 745
Woodgate, B. E., Robinson, R. D., Carpenter, K. G., Maran, S. P., & Shore, S. N. 1992, ApJ, 397, L95